Optimizing Relative Radiometric Normalization: Minimizing Residual Distortions in Multispectral Bitemporal Images Using Trust-Region Reflective and Laplacian Pyramid Fusion

Armin Moghimi, Turgay Celik, *Senior Member, IEEE*, Ali Mohammadzadeh, Saied Pirasteh, *Senior Member, IEEE*, and Jonathan Li, *Fellow, IEEE*

***Abstract*— Accurate relative radiometric normalization (RRN) is important for reliable multitemporal remote sensing image analysis. Traditional methods often depend on coregistered image pairs, limiting their applicability with unregistered data. Keypoint-based RRN (KRRN) relaxes this constraint but remains affected by residual radiometric errors due to normalization inaccuracies and nonlinear effects. This letter introduces a refinement strategy that leverages the trust-region reflective (TRR) algorithm to optimize normalization parameters, coupled with Laplacian pyramid (LP) fusion for seamless image integration. Evaluation on four multispectral image pairs from different sensors (e.g., Landsat 8 and Sentinel-2, IRS and Landsat 5, Landsat 7 and SPOT-5, and UK-DMC2 and Landsat 5) and one pair from the same sensor (Sentinel-2) showed that our method reduces residual radiometric discrepancies, achieving up to 29% lower RMSE than some well-known models. The source code and datasets are available on GitHub: https://github.com/ArminMoghimi/Tensor-based-keypoint-detection**

***Index Terms*— Laplacian pyramid (LP), multispectral satellite images, radiometric normalization, trust-region reflective (TRR).**

I. Introduction

RADIOMETRIC inconsistencies in bitemporal multispectral images, caused by atmospheric and calibration differences, hinder change detection (CD) and image mosaicking [1], [2]. Relative radiometric normalization (RRN) addresses these issues by aligning subject and reference images using pseudoinvariant features (PIFs)/inliers [3]. Iteratively reweighted multivariate alteration detection (IR-MAD) [4] is a widely adopted RRN method for CD. Recent rule-based approaches have also shown robust performance in cross-sensor images [5], [6], [7]. Most conventional RRN methods are limited by their dependence on preregistered image pairs, reducing their effectiveness in unregistered scenarios. Although deep learning approaches, such as the weakly supervised RS-NormGAN model [8], improve radiometric normalization for CD, they require large training data and still depend on registration. Keypoint-based RRN (KRRN) models address this challenge using image matching techniques to correct radiometric distortions in both registered and unregistered images, allowing simultaneous registration and radiometric correction [2], [9]. However, challenges remain, including sparse correspondences that hinder accurate parameter estimation and image warping during registration, which can affect accuracy. Nonlinear modeling approaches offer potential solutions, but must balance performance and overfitting risks, particularly with sparse inliers. Metaheuristic methods, such as genetic algorithms [10], have also been proven effective for parameter optimization, but they are computationally intensive.

This letter introduces an optimized radiometric normalization pipeline combining trust-region reflective (TRR) (for bounded parameter refinement) and Laplacian pyramid (LP) fusion (for artifact-free blending) to address residual radiometric distortions in multispectral image pairs. TRR was selected for its ability to handle nonlinear least-squares problems and enforce bound constraints [11], making it ideal for fine-tuning normalization parameters. Our method identifies reliable inliers using a combined change index (CI) from reference and initial normalized KRRN images refine the normalization parameters with TRR, and it integrates the results using the LP approach to minimize residual radiometric distortions.

II. Material and Methods

A. Methodology

The optimization process, illustrated in Fig. 1, consists of three key steps designed to minimize residual radiometric errors in the KRRN process.

Received 11 January 2025; revised 12 March 2025; accepted 9 April 2025. Date of publication 18 April 2025; date of current version 30 April 2025. *(Corresponding author: Armin Moghimi.)*

Armin Moghimi and Ali Mohammadzadeh are with the Department of Photogrammetry and Remote Sensing, K. N. Toosi University of Technology, Tehran 15875-4416, Iran (e-mail: moghimi.armin@gmail.com; a_mohammadzadeh@kntu.ac.ir).

Turgay Celik is with the School of Electrical and Information Engineering, University of the Witwatersrand, Johannesburg 2000, South Africa, and also with the Faculty of Engineering and Science, University of Agder, 4604 Kristiansand, Norway (e-mail: celikturgay@gmail.com).

Saied Pirasteh is with the Institute of Artificial Intelligence, Shaoxing University, Shaoxing, Zhejiang 312000, China, and also with the Department of Geotechnics and Geomatics, Saveetha School of Engineering, Saveetha Institute of Medical and Technical Sciences, Chennai, Tamil Nadu 600077, India (e-mail: sapirasteh1@usx.edu.cn).

Jonathan Li is with the Department of Geography and Environmental Management and the Department of Systems Design Engineering, University of Waterloo, Waterloo, ON N2L 3G1, Canada (e-mail: junli@uwaterloo.ca).

This article has supplementary downloadable material available at https://doi.org/10.1109/LGRS.2025.3562276, provided by the authors.

Digital Object Identifier 10.1109/LGRS.2025.3562276

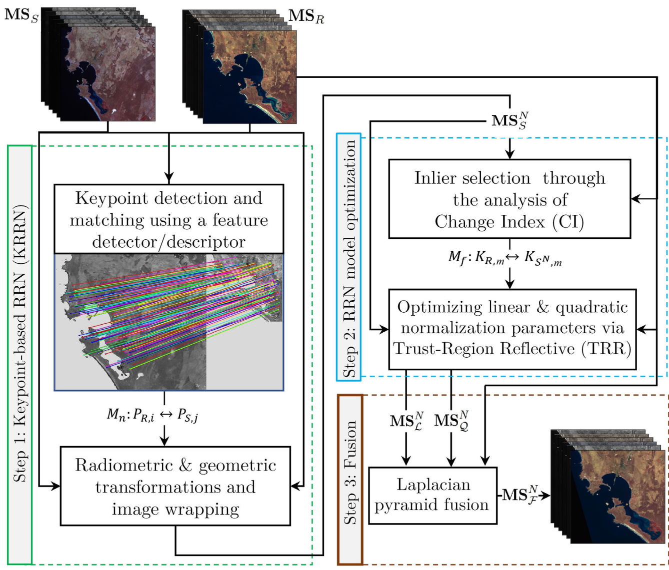

Fig. 1. Workflow of the proposed KRRN optimization approach.

1) Step 1: Keypoint-Based RRN: Consider unregistered bitemporal multispectral images $\mathbf{MS}_R \in \mathbb{R}^{H_R \times W_R \times C}$ (reference) and $\mathbf{MS}_S \in \mathbb{R}^{H_S \times W_S \times C}$ (subject), where H_R, W_R and H_S, W_S represent the height and width, and C refers to the number of spectral channels of the reference and subject images, respectively. The goal of KRRN methods is to generate a normalized subject image $\mathbf{MS}_S^N \in \mathbb{R}^{H_R \times W_R \times C_R}$, which is geometrically aligned and radiometrically normalized to match $\mathbf{MS}_R$. This process minimizes the error between keypoint matches $M_n(P_{R,i}, P_{S,j})$ under a geometric transformation $\mathbf{T}_g$, where $P_{R,i}$ and $P_{S,j}$ are the ith and jth keypoints in the reference and subject images, respectively. Radiometric normalization minimizes the difference in digital numbers (DNs) for these matches using a transformation $\mathbf{T}_r$, given by $\min_{\mathbf{T}_r} \sum_{k=1}^{N} \|\mathrm{DN}_{P_{R,k,c}} - \mathbf{T}_r(\mathrm{DN}_{P_{S,k,c}})\|_2^2$, where $\|\cdot\|_2^2$ denotes the *squared Euclidean norm* (L2 norm), and $\mathrm{DN}_{P_{R,k,c}}$ and $\mathrm{DN}_{P_{S,k,c}}$ represent the DNs of the kth matched keypoint in the cth band of the reference and subject images, respectively. The transformation $\mathbf{T}_r$ can be represented by the polynomial function $\mathbf{T}_r(\mathrm{DN}_{P_{S,k,c}}) = \sum_{d=0}^{D} a_d (\mathrm{DN}_{P_{S,k,c}})^d$, where a_d are the polynomial coefficients, and D is the maximum degree of the polynomial (for $D = 1$ (linear), the coefficients are a_0 and a_1; for $D = 2$ (quadratic), the coefficients are a_0, a_1, and a_2). After determining the geometric and radiometric transformations, they are applied jointly ($\mathbf{T} = \mathbf{T}_g \circ \mathbf{T}_r$) to obtain the co-registered normalized image $\mathbf{MS}_S^N$ through image warping. Here, an affine transformation was used for geometric correction, while a linear model was used for radiometric normalization.

2) Step 2: RRN Model Optimization: To minimize residual errors in the normalized image $\mathbf{MS}_S^N$, we apply an optimization approach. This step uses the normalized magnitude of change vector analysis (CVA) and dissimilarity derived from cosine similarity (CS) between the overlapping areas of $\mathbf{MS}_R$ and $\mathbf{MS}_S^N$ to compute the CI

$$\mathbf{CI} = \frac{\left(\frac{\mathbf{CVA}}{\max(\mathbf{CVA})} + \left(1 - \frac{\mathbf{CS}+1}{2}\right)\right)}{2}. \tag{1}$$

The CI is then segmented into change and no-change areas using multilevel Otsu thresholding, creating a change map (CM), where CM $\in \{0, 1\}$ (with 0 for changed areas and 1 for unchanged areas). A subset of spatially distributed inliers, denoted $M_f = \{M_f(K_{R,m}, K_{S^N,m}) \mid m = 1, \ldots, N_f\}$, are selected from the no-change areas of the CM, where N_f represents the total number of inliers and is chosen by $2 \times \mathrm{Min}(H_R, W_R)$. These inliers are then used to estimate more accurate normalization coefficients (Θ_r) through TRR optimization, with the objective function $F(\Theta_r) = \sum_{m=1}^{N_f} \|\mathrm{DN}_{K_{R,m,c}} - \mathbf{T}_r(\mathrm{DN}_{K_S^N,m,c})\|^2$, where DN_{K_R} and $\mathrm{DN}_{K_S^N}$ are the DNs for the inliers in the cth channel of $\mathbf{MS}_R$ and $\mathbf{MS}_S^N$, respectively. Within a trust region Δ, the TRR algorithm uses the quadratic model $Q(\Theta_r, p)$ to approximate the objective function $F(\Theta_r)$ as

$$Q(\Theta_r, p) = \frac{1}{2} p^T B p + (\nabla F(\Theta_r))^T p \tag{2}$$

where B is a positive definite matrix, p is the update vector, and $\nabla F(\Theta_r)$ is the gradient of the objective function evaluated at the current parameter values. TRR optimizes $\nabla F(\Theta_r)$ by solving

$$\min_{\Delta\Theta_r} Q(\Theta_r, p), \quad \text{s.t. } \|p\| \leq \Delta. \tag{3}$$

The trust region size is dynamically adjusted based on the ratio of predicted to actual reductions in the objective function $F(\Theta_r)$. As radiometric distortions are mostly handled in initial RRN modeling, the optimized parameters align with the initial fits and the trust region is here constrained by bounds

$$\mathbf{lb} = [a_d - \Delta a_d], \quad \mathbf{ub} = [a_d + \Delta a_d] \tag{4}$$

where **lb** and **ub** are the lower and upper bounds, respectively, a_d are the fitting coefficients, and $\Delta a_d = 0.05$ ensures proper constraints. The optimization process terminates when the change in the objective function value falls below a threshold of 10^{-6}. After optimizing linear and quadratic parameters with TRR, the normalized images $\mathbf{MS}_{\mathcal{L}}^N$ and $\mathbf{MS}_{\mathcal{Q}}^N$ are generated.

3) Step 3: Fusion: To ensure accurate normalization, the normalized images $\mathbf{MS}_{\mathcal{L}}^N$ and $\mathbf{MS}_{\mathcal{Q}}^N$ are fused using the LP strategy based on $\mathbf{MS}_R$, resulting in the fused image $\mathbf{MS}_{\mathcal{F}}^N$. For each pyramid level l, the Laplacian levels are computed by

$$L_X^l = Z_X^{l-1} - \mathrm{upsample}\left(Z_X^l\right), \quad X \in \left\{\mathbf{MS}_{\mathcal{L}}^N, \mathbf{MS}_{\mathcal{Q}}^N, \mathbf{MS}_R\right\} \tag{5}$$

where Z_X^l denotes the non-Gaussian pyramid levels, capturing progressively lower frequency image details. The gradient differences and corresponding weights are then calculated, respectively, by $\Delta_X^l = L_X^l - L_{\mathbf{MS}_R}^l$, and $w_X^l = (1/((\Delta_X^l)^2 + \epsilon))$, where $X \in \{\mathbf{MS}_{\mathcal{L}}^N, \mathbf{MS}_{\mathcal{Q}}^N\}$, and $\epsilon = 2.2 \times 10^{-16}$ is used to avoid division by zero. The fused image levels are formed by $L_{\mathbf{MS}_{\mathcal{F}}^N}^l = ((w_{\mathcal{L}}^l L_{\mathbf{MS}_{\mathcal{L}}^N}^l + w_{\mathcal{Q}}^l L_{\mathbf{MS}_{\mathcal{Q}}^N}^l)/(w_{\mathcal{L}}^l + w_{\mathcal{Q}}^l))$. The fused image is then reconstructed by upsampling and adding layers

$$\mathbf{MS}_{\mathcal{F}}^N = L_{\mathbf{MS}_{\mathcal{F}}^N}^L + \sum_{l=1}^{L-1} \mathrm{upsample}\left(L_{\mathbf{MS}_{\mathcal{F}}^N}^l\right). \tag{6}$$

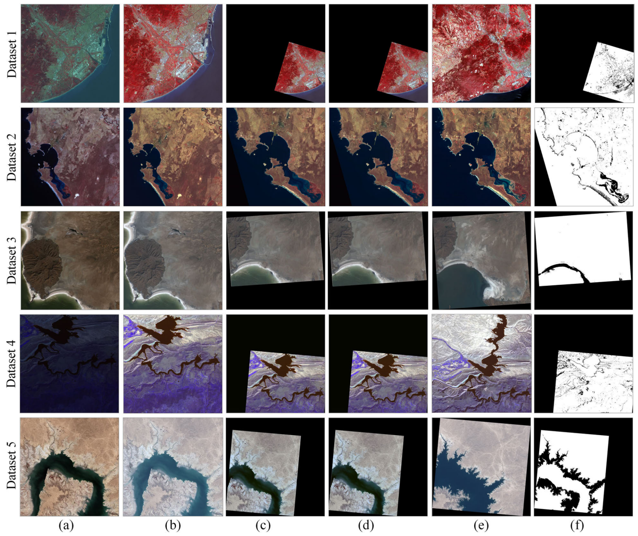

Fig. 2. (a) Subject images, (b) normalized images by KRRN, (c) and (d) co-registered normalized images produced by the proposed method, which combines TRR and GA with the LP (i.e., (c) KRRN-FTRR$_{\mathcal{L},\mathcal{Q}}$, and (d) KRRN-FGA$_{\mathcal{L},\mathcal{Q}}$). (e) reference images, and (f) ground-truth maps (white: unchanged, black: changed, no data).

To ensure a balanced fusion and minimize discrepancies with the reference image, the fused image $\mathbf{MS}_{\mathcal{F}}^N$ is defined as follows:

$$\mathbf{MS}_{\mathcal{F}}^N = \frac{w_{\mathcal{F}}\mathbf{MS}_{\mathcal{F}}^N + w_{\mathcal{L}}\mathbf{MS}_{\mathcal{L}}^N + w_{\mathcal{Q}}\mathbf{MS}_{\mathcal{Q}}^N}{w_{\mathcal{F}} + w_{\mathcal{L}} + w_{\mathcal{Q}}} \tag{7}$$

where $w_X = (1/((\mathbf{MS}_X^N - \mathbf{MS}_R)^2 + \epsilon))$ are the weights defined for $X \in \{\mathcal{F}, \mathcal{L}, \mathcal{Q}\}$. For our approach, the number of pyramid levels L is determined by

$$L = \max\left(2, 1 + \left|\frac{L_{\max} - \max(E_{\mathbf{MS}_R}, E_{\mathbf{MS}_S^N})}{\mathrm{mean}(E_{\mathbf{MS}_R}, E_{\mathbf{MS}_S^N}) + \min(E_{\mathbf{MS}_R}, E_{\mathbf{MS}_S^N}) + 1}\right|\right) \tag{8}$$

where $L_{\max} = (\lfloor \log_2(\min(H_R, W_R)) \rfloor / 4)$, and $E_{\mathbf{MS}_R}$ and $E_{\mathbf{MS}_S^N}$ represent the entropy values of the reference and normalized subject images, respectively. The detailed steps of the proposed methodology are outlined in Algorithm 1.

B. Dataset

We used five sets of bitemporal multispectral images from various sensors and conditions for evaluation (see Table I and Fig. 2(a) and (e); see [2] for details). All the reference images were atmospherically corrected, and both the reference and subject images are not co-registered. Sentinel-2 images were resampled to a 10-m resolution. Image pairs in Datasets 2 and 4 have pixel size differences of 8 and 6 m, respectively, while Datasets 1 and 3 have a threefold spatial resolution difference. Ground-truth maps for overlapping areas were created with Otsu thresholding and postprocessed via photointerpretation to assess RRN performance [see Fig. 2(f)].

Algorithm 1 Proposed KRRN Optimization Approach

Input : $\mathbf{MS}_R$ (reference), and $\mathbf{MS}_S$ (subject)
Output: $\mathbf{MS}_{\mathcal{L}}^N$, $\mathbf{MS}_{\mathcal{Q}}^N$, $\mathbf{MS}_{\mathcal{F}}^N$
Data : Constraints: $\mathbf{lb} = [a_i - \Delta a_d]$, $\mathbf{ub} = [a_d + \Delta a_d]$, where $\Delta a_d = 0.05$ for $d = 0, 1, 2$

Step 1: KRRN

- Keypoint Matching

Detect keypoints: $P_R \subset \mathbf{MS}_R$, $P_S \subset \mathbf{MS}_S$
Match keypoints: $M_n(P_R, P_S)$

- Geometric and Radiometric Transformation

$\mathbf{T}_g \leftarrow M_n(P_R, P_S)$ & $\mathbf{T}_r \leftarrow \mathrm{DN}_{P_{R,k,c}}, \mathrm{DN}_{P_{S,k,c}}$
$\mathbf{MS}_S^N \xleftarrow{\mathbf{T}=\mathbf{T}_g \circ \mathbf{T}_r} \mathbf{MS}_S$

Step 2: RRN Model Optimization

- Inlier Detection

$\mathbf{CM} \xleftarrow{\text{Thresholding}} \mathbf{CI} \xleftarrow{(1)} \mathbf{MS}_R, \mathbf{MS}_S^N$
Inliers: $M_f(K_{R,i}, K_{S^N,i}) \xleftarrow{N_f = 2\times\min(H_R, W_R)} \mathbf{CM}$

- TRR Optimization Algorithm

Define $F(\Theta_r)$ and Initialize Θ_r and Δ
while *not converged* **do**
  Compute $Q(\Theta_r, p)$ using (2)
  Solve $\|p\| \leq \Delta$ using (3)
  Update Θ_r

Step 3: Fuse Normalized Images

Compute $\mathbf{MS}_{\mathcal{L}}^N$, $\mathbf{MS}_{\mathcal{Q}}^N$ using optimized parameters Θ_r
for $c = 1$ ***to*** C **do**
  Compute $E_{\mathbf{MS}_{R,c}}$, $E_{\mathbf{MS}_{S,c}^N}$, $L_{\max}$, and set L using (8);
  Construct LPs for $\mathbf{MS}_{\mathcal{L},c}^N$, $\mathbf{MS}_{\mathcal{Q},c}^N$, and $\mathbf{MS}_{R,c}$;
  for $l = 1$ ***to*** L **do**
    Compute differences $\Delta_{\mathcal{L},c}^l$, $\Delta_{\mathcal{Q},c}^l$ and weights $w_{\mathcal{L},c}^l$, $w_{\mathcal{Q},c}^l$;
    Compute fused pyramid level $L_{\mathbf{MS}_{\mathcal{F},c}^N}^l$;
  Reconstruct $\mathbf{MS}_{\mathcal{F},c}^N$ and calculate final weights using (6) & (7);

return $\mathbf{MS}_{\mathcal{L}}^N$, $\mathbf{MS}_{\mathcal{Q}}^N$, $\mathbf{MS}_{\mathcal{F}}^N$

III. Experimental Design and Evaluation

In our experiments, WSST-SURF [2] was used for registration and initial RRN via inlier detection. Experiments were run in MATLAB 2018b a Windows 10 machine with an Intel Core i7-9750H CPU and 16-GB RAM.

Optimization performance was evaluated using average root mean square error (RMSE) and structural similarity index (SSIM) (on unchanged overlapping pixels), and processing time for TRR and Laplacian fusion, compared with GA-based optimization on baseline KRRN (see Section III-A and Fig. 3). We also compared results with LIRRN [12], RS-RRN [13], and GMM-RRN [6] using RMSE and CD total error rate (TER) (see Section III-B, Table II, and Fig. 4). In our experiments, direct renormalizations of KRRN using TRR for

TABLE I
DATASETS' CHARACTERISTICS

Dataset	Ref./ Sub. Image	Satellite	Common Spectral band	Spatial Res. (m)	Radiometric Res. (in bits)	Image size (in pixels)	Date	Study Area
#1	$\mathbf{MS}_R$	SPOT-5	Green, Red, NIR, SWIR	10	8	2000 × 2000	May-2007	Barcelona,
	$\mathbf{MS}_S$	Landsat 7 (ETM+)		30		1300 × 1300	May-2000	Spain
#2	$\mathbf{MS}_R$	UK-DMC2	Green, Red,	22	8	1000 × 1000	Feb-2012	Cape Town, South Africa
	$\mathbf{MS}_S$	Landsat 5 (TM)	NIR,	30		2000 × 2000	Feb-2007	
#3	$\mathbf{MS}_R$	Sentinel-2 (MSI)	C/A, Blue, Green, Red,	10/20/60	12	1602 × 1601	Jul-2019	Shahi Island,
	$\mathbf{MS}_S$	Landsat 8 OLI	NIR, SWIR1, SWIR 2	30	16	1300 × 1300	Sep-2019	Iran
#4	$\mathbf{MS}_R$	Landsat 5 (TM)	Green, Red,	30	8	1000 × 1000	Jul-2009	Daggett County, USA
	$\mathbf{MS}_S$	IRS (LISS IV)	NIR, SWIR	24		1000 × 1000	Jun-2020	
#5	$\mathbf{MS}_R$	Sentinel-2 (MSI)	C/A, Blue, Green, Red, RE 1-3,	10/20/60	12	1625 × 1625	Oct-2016	Haditha dam,
	$\mathbf{MS}_S$		NIR, NIRn, WV, SWIR1, SWIR 2			1500 × 1500	Aug-2015	Iraq

NIR=Near Infra-Red SWIR= Short Wavelength Infra-Red RE=Red-Edge C/A=Coastal Aerosol NIRn=Narrow NIR WV=Water Vapour

TABLE II
COMPARATIVE ANALYSIS OF RRN METHODS: AVERAGE RMSE AND CD TER (%) RESULTS ACROSS DATASETS 1–5

Method	#1 RMSE	#1 TER	#2 RMSE	#2 TER	#3 RMSE	#3 TER	#4 RMSE	#4 TER	#5 RMSE	#5 TER
Raw	54.14	–	20.51	–	1E4	–	90.35	–	205.13	–
LIRRN [12]	35.48	17.69	9.38	2.75	322.56	1.76	16.54	5.15	129.66	1.79
RS-RRN [13]	37.80	17.32	9.39	1.66	308.08	0.88	16.83	3.11	125.26	1.67
GMM-RRN [6]	38.52	17.87	9.42	1.89	330.55	0.91	20.45	3.97	128.37	1.74
KRRN-FTRR$_{\mathcal{L},\mathcal{Q}}$	**33.48**	**16.25**	**9.13**	**1.59**	**297.36**	**0.84**	**14.45**	**2.49**	**118.68**	**1.13**

linear and quadratic models were denoted as DKRRN-TRR$_{\mathcal{L}}$ and DKRRN-TRR$_{\mathcal{Q}}$. Further optimizations with TRR and GA are labeled as KRRN-TRR$_{\mathcal{L}}$, KRRN-TRR$_{\mathcal{Q}}$, KRRN-GA$_{\mathcal{L}}$, and KRRN-GA$_{\mathcal{Q}}$. Joint optimizations combining TRR and GA with LP fusion are referred to as KRRN-FTRR$_{\mathcal{L},\mathcal{Q}}$ and KRRN-FGA$_{\mathcal{L},\mathcal{Q}}$, respectively. TRR used MATLAB's `lsqcurvefit` with `optimoptions`; GA used `ga` with a 1×10^{-6} constraint tolerance over 20 generations. Default parameters were used for LIRRN, RS-RRN, and GMM-RRN as per their respective papers. CD maps were obtained by calculating the magnitude of CVA using co-registered normalized and reference images, followed by Otsu's thresholding.

A. RRN Optimization Evaluation

As shown in Fig. 3, KRRN-FTRR$_{\mathcal{L},\mathcal{Q}}$ achieved the best performance across all the datasets, with KRRN-FGA$_{\mathcal{L},\mathcal{Q}}$ closely following. This highlights the benefit of combining TRR/GA with LP fusion in reducing radiometric differences. RMSE improvements ranged from 8% (Dataset 2) to 14% (Dataset 5), with smaller gains in SSIM. In contrast, using only TRR or GA (KRRN-GA/TRR$_{\mathcal{L}}$, KRRN-GA/TRR$_{\mathcal{Q}}$) resulted in modest improvements, while DKRRN-TRR$_{\mathcal{L}}$, DKRRN-TRR$_{\mathcal{Q}}$, and the baseline KRRN showed inconsistent or inferior results. Furthermore, replacing TRR with GA increased computation time by 2–3× without improving accuracy (see Figs. 2 and 3), reinforcing the superiority of TRR in RRN optimization.

B. Comparative Results of the RRN Methods

While visual differences in the normalized images are subtle (see Fig. 4), quantitative results confirm the superior performance of KRRN-FTRR$_{\mathcal{L},\mathcal{Q}}$. As shown in Table II, it consistently outperformed LIRRN, RS-RRN, and GMM-RRN in RMSE and CD TRE across all the datasets. Compared

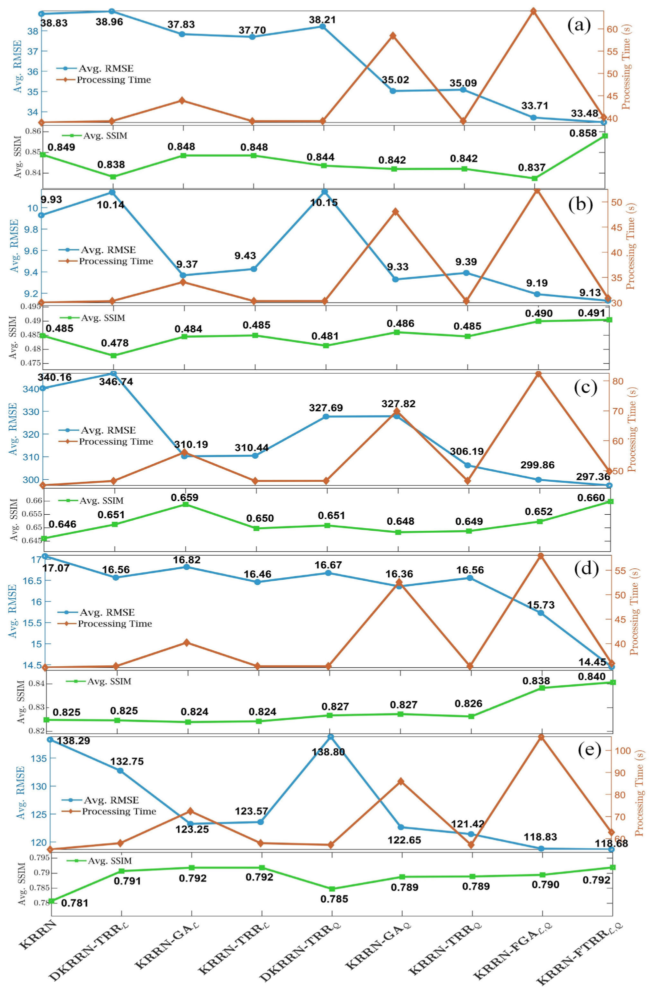

Fig. 3. Comparison of KRRN performance before and after direct renormalization with matched keypoints and the proposed optimization strategy (TRR versus GA) for Datasets 1–5 (a)–(e).

with LIRRN, RS-RRN, and GMM-RRN, the proposed method achieved significant improvements, reducing RMSE by up to 12.64%, 14.14%, and 29.33% in the best case (Dataset 3) and by up to 2.67%, 2.77%, and 3.08% in the worst case (Dataset 2), respectively. Furthermore, it also achieved the lowest TRE, outperforming LIRRN, RS-RRN, and GMM-RRN by up to 2.66%, 0.62%, and 1.48% in the best case (Dataset 4) and 0.6% in the worst case (Dataset 5), respectively.

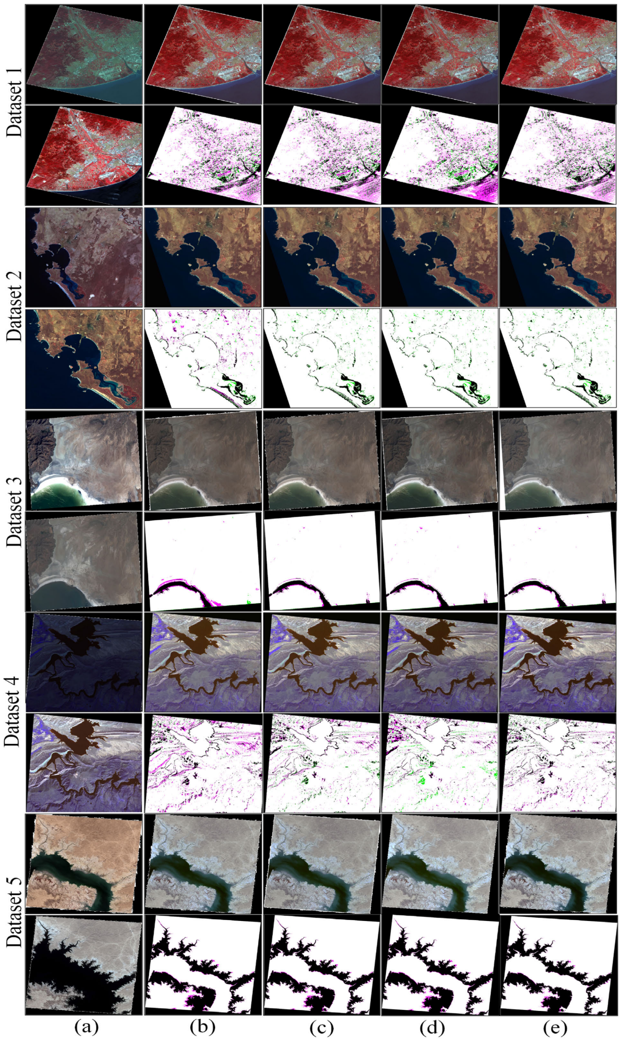

Fig. 4. (Top row) Normalized images and (bottom row) overlaid ground-truth and CD maps generated by (b) LIRRN, (c) RS-RRN, (d) GMM-RRN, and (e) KRRN-FTRR$_{\mathcal{L},\mathcal{Q}}$A for the subject (top row) and reference (bottom row) test images in (a). Legend of overlaid CD maps: green = false alarms, pink = missed detections.

CD maps in Fig. 4 further support these results, showing that the proposed method achieved the lowest false and miss detection errors, particularly in Datasets 2 and 4. These findings highlight the method's effectiveness in reducing residual radiometric errors, especially in challenging cases like Dataset 3 (16-bit vs. 12-bit), while maintaining robust performance overall.

IV. Conclusion

The letter presented an optimized KRRN strategy that integrates TRR and LP fusion, effectively improving radiometric alignment and reducing residual distortions across five datasets. TRR showed greater computational efficiency than GA, and its combination with LP fusion achieved lower RMSE and superior CD performance compared with some state-of-the-art methods. While effective on mid-resolution imagery, extending our approach to high-resolution data requires further study. Although inliers were autoselected in our process, performance still depended on their accurate identification after KRRN processing. However, our framework's modularity supports integration with other RRN methods, with room for enhancement via advanced evolutionary and fusion techniques.

References

[1] S. Zhengguang, L. Zhijiang, and C. Liqin, "An illumination normalization method for Antarctic remote sensing images," *Remote Sens. Lett.*, vol. 16, no. 3, pp. 253–263, Mar. 2025.

[2] A. Moghimi, T. Celik, and A. Mohammadzadeh, "Tensor-based keypoint detection and switching regression model for relative radiometric normalization of bitemporal multispectral images," *Int. J. Remote Sens.*, vol. 43, no. 11, pp. 3927–3956, Jun. 2022.

[3] W. Huang, Y. Tao, W. Gan, and H. Shen, "An evaluation of radiometric normalization methods for Gaofen-2 vegetation index mapping," *IEEE Geosci. Remote Sens. Lett.*, vol. 21, pp. 1–5, 2024.

[4] M. J. Canty and A. A. Nielsen, "Automatic radiometric normalization of multitemporal satellite imagery with the iteratively re-weighted MAD transformation," *Remote Sens. Environ.*, vol. 112, no. 3, pp. 1025–1036, Mar. 2008.

[5] H. Xu, Y. Zhou, Y. Wei, H. Guo, and X. Li, "A multirule-based relative radiometric normalization for multisensor satellite images," *IEEE Geosci. Remote Sens. Lett.*, vol. 20, pp. 1–5, 2023.

[6] H. Ghanbari, S. Homayouni, P. Ghamisi, and A. Safari, "Radiometric normalization of multitemporal and multisensor remote sensing images based on a Gaussian mixture model and error ellipse," *IEEE J. Sel. Topics Appl. Earth Observ. Remote Sens.*, vol. 11, no. 11, pp. 4526–4533, Nov. 2018.

[7] H. Xu, Y. Wei, X. Li, Y. Zhao, and Q. Cheng, "A novel automatic method on pseudo-invariant features extraction for enhancing the relative radiometric normalization of high-resolution images," *Int. J. Remote Sens.*, vol. 42, no. 16, pp. 6153–6183, Aug. 2021.

[8] J. Miao, S. Li, X. Bai, W. Gan, J. Wu, and X. Li, "RS-NormGAN: Enhancing change detection of multi-temporal optical remote sensing images through effective radiometric normalization," *ISPRS J. Photogramm. Remote Sens.*, vol. 221, pp. 324–346, Mar. 2025.

[9] T. Kim and Y. Han, "Integrated preprocessing of multitemporal very-high-resolution satellite images via conjugate points-based pseudo-invariant feature extraction," *Remote Sens.*, vol. 13, no. 19, p. 3990, Oct. 2021.

[10] G. Kumar, A. Kumar, and R. Gupta, "Relative radiometric normalization for mosaicking IRS CartoSat-2 panchromatic images using genetic algorithm," *Geocarto Int.*, vol. 37, no. 26, pp. 11614–11632, Dec. 2022.

[11] G. H. Cheng, A. Younis, K. H. Hajikolaei, and G. G. Wang, "Trust region based mode pursuing sampling method for global optimization of high dimensional design problems," *J. Mech. Design*, vol. 137, no. 2, Feb. 2015, Art. no. 021407.

[12] A. Moghimi, V. Sadeghi, A. Mohsenifar, T. Celik, and A. Mohammadzadeh, "LIRRN: Location-independent relative radiometric normalization of bitemporal remote-sensing images," *Sensors*, vol. 24, no. 7, p. 2272, Apr. 2024.

[13] W. Bonnet and T. Celik, "Random sampling-based relative radiometric normalization," *IEEE Geosci. Remote Sens. Lett.*, vol. 19, pp. 1–4, 2022.